A&A 465, 879–885 (2007)
DOI: 10.1051/0004-6361:20066625
© ESO 2007

Astronomy & Astrophysics

High resolution simulations of a variable HH jet

A. C. Raga[1], F. De Colle[2], P. Kajdič[3], A. Esquivel[1], and J. Cantó[3]

[1] Instituto de Ciencias Nucleares, Universidad Nacional Autónoma de México, Ap. 70-543, 04510, DF México
e-mail: [raga;esquivel]@nucleares.unam.mx
[2] Dublin Institute of Advanced Studies, 5 Merrion Sq., Dublin, Ireland
e-mail: fdc@cp.dias.ie
[3] Instituto de Astronomía, Universidad Nacional Autónoma de México, Ap. 70-264, 04510, DF México
e-mail: primoz@astroscu.unam.mx

Received 24 October 2006 / Accepted 30 December 2006

ABSTRACT

Context. In many papers, the flows in Herbig-Haro (HH) jets have been modeled as collimated outflows with a time-dependent ejection. In particular, a supersonic variability of the ejection velocity leads to the production of "internal working surfaces" which (for appropriate forms of the time-variability) can produce emitting knots that resemble the chains of knots observed along HH jets.
Aims. In this paper, we present axisymmetric simulations of an "internal working surface" in a radiative jet (produced by an ejection velocity variability). We concentrate on a given parameter set (i.e., on a jet with a constante ejection density, and a sinusoidal velocity variability with a 20 yr period and a 40 km s^{-1} half-amplitude), and carry out a study of the behaviour of the solution for increasing numerical resolutions.
Methods. In our simulations, we solve the gasdynamic equations together with a 17-species atomic/ionic network, and we are therefore able to compute emission coefficients for different emission lines.
Results. We compute 3 adaptive grid simulations, with 20, 163 and 1310 grid points (at the highest grid resolution) across the initial jet radius. From these simulations we see that successively more complex structures are obtained for increasing numerical resolutions. Such an effect is seen in the stratifications of the flow variables as well as in the predicted emission line intensity maps.
Conclusions. We find that while the detailed structure of an internal working surface depends on resolution, the predicted emission line luminosities (integrated over the volume of the working surface) are surprisingly stable. This is definitely good news for the future computation of predictions from radiative jet models for carrying out comparisons with observations of HH objects.

Key words. methods: numerical – ISM: general – ISM: jets and outflows – ISM: Herbig-Haro objects

1. Introduction

Over the last two decades, a relatively large number of papers have presented numerical simulations of radiative jets. Axisymmetric and 3D models have been computed with parametrized cooling functions (as, e.g., in the old papers of Raga 1988; Blondin et al. 1989), with cooling rates calculated as a function of the computed (non-equilibrium) abundances of $1 \rightarrow 3$ species (e.g., Biro & Raga 1994; Smith et al. 1997; Downes & Ray 1998), or with $\sim 10 \rightarrow 20$ species (Raga et al. 2002a, 2004). The more recent 1D time-dependent simulations of jets (Massaglia et al. 2005) use the (cleverly devised) simple cooling function of Hartigan & Raymond (1993), and do not carry out a more detailed treatment of the ionization and cooling (as was done, e.g., in the 1D time-dependent shock models of Innes et al. 1987a,b).

Recently, there have been a number of papers with 2 and 3D simulations of jets with a detailed enough treatment of the atomic/ionic (Raga et al. 2004; Kajdič et al. 2006) and chemical (Smith & Rosner 2005; Raga et al. 2005) structure in order to obtain predictions of the emission of a set of different emission lines. The simulations with by far the largest chemical detail up to date are the ones of Lim et al. (1999, 2001). These simulations have been carried out with numerical resolutions in the range of 10 to 100 grid points across the jet radius (and with cooling distances resolved with only 1 to 10 points).

In the present paper we address the point of what kind of numerical resolution is actually necessary in order to produce reliable predictions of the flow structure and emission properties of radiative jets. Such a study has been attempted before for non-radiative jets (Kössl & Müller 1988). For the case of radiative jets, such a study has not yet been described, but very high spatial resolution simulations of individual working surfaces have been carried out by Falle & Raga (1993, 1995).

In the present work, we concentrate on a radiative jet model with a variable ejection velocity, which results in the production of a number of "internal working surfaces" travelling down the jet flow (see Raga et al. 1990). We carry out adaptive grid simulations in which we focus on a single internal working surface, and follow it at high spatial resolution, with the rest of the jet flow solved at a substantially lower resolution.

These simulations are of course similar to the single internal working surface simulations of Falle & Raga (1993, 1995), who applied boundary conditions so as to keep the internal working surface within a spatially limited computational domain, and to the ones of Biro (1996), who applied periodic axial boundary conditions. However, the simulation described in the present paper also includes a calculation of the full jet flow (albeit at a not so high spatial resolution) and its influence on the internal working surface. Also, our present simulations include a 17-species atomic/ionic network (only simple, parametrized cooling functions were used by Falle & Raga 1993, 1995; and by Biro 1996),

Article published by EDP Sciences and available at http://www.aanda.org or http://dx.doi.org/10.1051/0004-6361:20066625

which allows us to carry out predictions of the emission line spectrum.

The physical model and the computational configuration used for our simulations is described in Sect. 2. The parameters for the three computed simulations are described in Sect. 3. The flow stratifications obtained from three simulations (of increasing spatial resolutions) are described in Sect. 4. The Hα and [O I] 6300 emission is discussed in Sect. 5. The results are summarized in Sect. 6.

2. The physical/numerical model

2.1. Context

In this paper, we give a description of the gasdynamic code (Sect. 2.2), the treatment of the non-equilibrium ionization and the radiative cooling (Sect. 2.3) and the physical and numerical setup (Sect. 2.4) used for computing the jet models. This description is intended as a guide for jet (or other types of ISM flow) code developers who are interested in including non-equilibrium ionization and radiative cooling in their codes.

2.2. The gasdynamic code

The models described in this paper were computed with a 2D, axisymmetric version of the "yguazú-a" code. This code integrates the gasdynamic equations together with a set of continuity+rate equations for a set of molecular/atomic/ionic species on a binary, adaptive grid.

The version of the yguazú-a code that has been used is basically identical to the original one, which was described in detail by Raga et al. (2000), so we refer the reader to this paper for a full description. This code was tested (in an unprecedented way for an astrophysically oriented code) with laboratory experiments of laser induced plasmas. The time-evolution of single shocks (Raga et al. 2000; Sobral et al. 2000), shock interactions (Velázquez et al. 2001) and jet-like flows (Raga et al. 2001) computed with the code have been quantitatively compared with experimental results, giving an evaluation of the reliability of the code for computing solutions to complex flows.

2.3. The atomic/ionic reaction set

The simulations have been computed considering continuity+rate equations for the atomic/ionic species: HI, HII, HeI, HeII, HeIII, CII, CIII, CIV, NI, NII, NIII, OI, OII, OIII, OIV, SII, and SIII. In other words, C and S are assumed to be at least singly ionized. We have used abundances of 0.9 (H), 0.1 (He), 3.31×10^{-4} (C), 9.8×10^{-5} (N), 6.61×10^{-4} (O) and 1.7×10^{-5} (S), by number, as fractions of the total number density of atoms+ions.

Even though we use the binary reaction coefficients for collisional ionization (by collisions with electrons), radiative+dielectronic recombination coefficients and charge exchange reactions available in the literature (from the thesis of Cox 1970, from Aldrovandi & Péquignot 1973, 1976; and from the book of Osterbrock 1989, respectively), we give a complete list of the interpolation formulae that we have used in Table 1, in order to facilitate implementation of the scheme in other codes. This is of particular relevance if the models that we are presenting are to be useful for comparisons between different radiative jet codes. A full description of the interpolation formulae used for all of the rate coefficients is given in Appendix A.

Table 1. Reaction rates.

Reaction	Coefficients[a]
e + HI → 2e + HII	1: 5.83×10^{-11}, 0.5, –157 800
e + HII → HI	1: 3.69×10^{-10}, –0.79, 0
e + HeI → 2e + HeII	1: 2.707×10^{-11}, 0.5, –285 400
e + HeII → HeI	2: 4.3×10^{-13}, 0.672, 0.0019, 4.7×10^{5}, 0.3, 94 000
e + HeII → 2e + HeIII	1: 5.711×10^{-12}, 0.5, –631 000
e + HeIII → HeII	1: 2.21×10^{-9}, –0.79, 0
e + CII → 2e + CIII	1: 3.93×10^{-11}, 0.5. –283 000
e + CIII → CII	2: 3.2×10^{-12}, 0.770, 0.038, 9.1×10^{4}, 2.0, 3.7×10^{5}
e + CIII → 2e + CIV	1: 2.04×10^{-11}, 0.5, –555 600
e + CIV → CIII	2: 2.3×10^{-12}, 0.645, 7.03×10^{-3}, 1.5×10^{5}, 0.5, 2.3×10^{5}
e + NI → 2e + NII	1: 6.18×10^{-11}, 0.5 –168 200
e + NII → NI	2: 1.5×10^{-12}, 0.693, 0.0031 2.9×10^{5}, 0.6, 1.7×10^{5}
e + NII → 2e + NIII	1: 4.21×10^{-11}, 0.5, –343 360
e + NIII → NII	2: 4.4×10^{-12}, 0.675, 0.0075 2.6×10^{5}, 0.7, 4.5×10^{5}
e + OI → 2e + OII	1: 1.054×10^{-10}, 0.5, –157 800
e + OII → OI	2: 2.0×10^{-12}, 0.646, 0.0014 1.7×10^{5}, 3.3, 5.8×10^{4}
e + OII → 2e + OIII	1: 3.53×10^{-11}, 0.5, –407 200
e + OIII → OII	2: 3.1×10^{-13}, 0.678, 0.0014 1.7×10^{5}, 2.5, 1.3×10^{5}
e + OIII → 2e + OIV	1: 1.656×10^{-11}, 0.5, –636 900
e + OIV → OIII	2: 5.1×10^{-12}, 0.666, 0.0028 1.8×10^{5}, 6.0, 91 000
e + SII → 2e + SIII	1: 7.12×10^{-11}, 0.5, –271 440
e + SIII → SII	2: 1.8×10^{-12}, 0.686, 0.0049 1.2×10^{5}, 2.5, 88 000
HI + NII → HII + NI	1: 1.1×10^{-12}, 0, 0
HII + NI → HI + NII	1: 4.95×10^{-12}, 0. –10 440
HI + OII → HII + OI	1: 2.0×10^{-9}, 0, 0
HII + OI → HI + OII	1: 1.778×10^{-9}, 0, –220

[a] The interpolation formulae are of the form "1": Arrhenius, or "2": Aldrovandi & Péquignot (1973), see Eqs. (A.1) and (A.2) in Appendix A.

2.4. The atomic/ionic cooling functions

We have included analytic interpolation formulae that give the low density regime cooling function for a number of atoms and ions. These cooling functions are described in full detail in the Appendix of the paper by Raga et al. (2002a), so we do not repeat them here.

The only difference between the cooling rates of the models of the present calculations and the ones of Raga et al. (2002a), is that we have not included the cooling due to H_2 emission, and that we have now added cooling functions for HeI and HeII:

$$L_{\rm HeI} = n_{\rm e} n_{\rm HeI}\, 10^{[-28.5+10.15(1-t)-50(1-t^{0.003})]}, \quad (1)$$

$$L_{\rm HeII} = n_{\rm e} n_{\rm HeII}\, 10^{[-28.1+20.40(0.5-t)-390(1-t^{0.0003})]}, \quad (2)$$

where $t = 10^4\ {\rm K}/T$, $n_{\rm e}$ is the electron density and $n_{\rm HeI}$, $n_{\rm HeII}$ are the HeI and HeII number densities, respectively. We have also included the free-free cooling of HeII and HeIII (with the formula given in the book of Osterbrock 1989) and the recombination cooling of these two ions (with the formula of Seaton 1959).

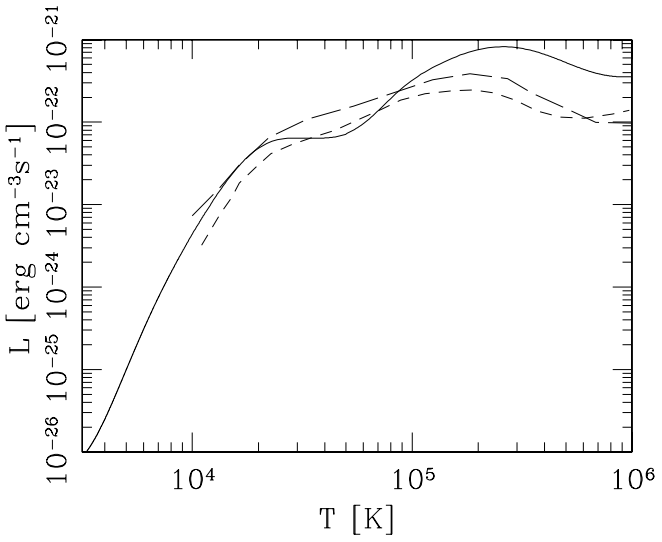

Fig. 1. Time-dependent cooling function (energy per unit volume and time) for an initially fully ionized parcel at $T = 10^6$ K, which cools at a constant $n = 1$ cm^{-3} atom+ion number density calculated with the ionization/cooling scheme described in the present paper (solid line). As a comparison, we show the equivalent curves computed by Innes et al. (1987a, short dashes) and by Shapiro & Moore (1976, long dashes).

In order to illustrate the behaviour of our reaction rate/cooling scheme, we have computed the time-dependent cooling function obtained for a parcel with a constant, $n = 1$ cm^{-3} number density, which cools from an initial temperature of 10^6 K. This cooling function (shown in Fig. 1) can be compared with equivalent cooling functions published in the literature (two curves taken from the literature are included as an example in Fig. 1).

3. The jet model

We consider an initially top-hat jet with a time-dependent ejection velocity of the form:

$$v_j(t) = \left[200 + 40 \sin\left(\frac{2\pi t}{20\,\mathrm{yr}}\right)\right] \mathrm{km\,s^{-1}}, \quad (3)$$

and a constant injection density $n_j = 1000$ cm^{-3}, temperature $T_j = 1000$ K and radius $r_j = 2 \times 10^{15}$ cm. The jet moves into a uniform environment of density $n_{\rm env} = 100$ cm^{-3} and temperature $T_{\rm env} = 1000$ K. Both the initial jet cross section and the undisturbed environment are neutral, except for C and S, which are singly ionized. These paremeters are chosen as representative of the ones that are found from comparisons between variable jet models and observations of HH jets (see, e.g., Raga et al. 2002b).

The simulations start at $t = 0$, with the jet beam having an initial length of 2×10^{15} cm. The integration continues giving the jet the time-dependent ejection velocity given by Eq. (3). This variable ejection velocity results in the production of a chain of two-shock "internal working surfaces" travelling down the jet beam.

We carry out three axisymmetric simulations at different spatial resolutions, in a computational domain with an axial extent of 10^{17} cm and a radial extent of 2.5×10^{16} cm. The simulations are carried out in the multi-level, binary adaptive grid of the "yguazú-a" code.

The three simulations share a 64×16 (axial×radial) uniform base grid. However, they differ in the number of binary grid refinements:

- **model M1:** has a 5-level grid structure, with a maximum resolution of 9.766×10^{13} cm (along the two axes);
- **model M2:** has an 8-level grid structure, with a maximum resolution of 1.221×10^{13} cm;
- **model M3:** has an 11-level grid structure, with a maximum resolution of 1.526×10^{12} cm.

These simulations would correspond to 1024×256 (M1), 8192×2048 (M2) and $65\,536 \times 16\,384$ (M3) points in a uniform grid at the highest resolution of the corresponding adaptive grids.

Models M1, M2 and M3 have 20, 163 and 1310 grid points across the jet radius (at the highest grid resolution). Also, it is interesting to mention that a stationary, plane-parallel shock wave with a preshock density of 1000 cm^{-3} and shock velocity of 40 km s^{-1} has a cooling distance (to 10^3 K, taken from the model tabulation of Hartigan et al. 1987) of $\approx 1.5 \times 10^{14}$ cm, which is then resolved by 1.5, 12 and 98 grid points in models M1, M2 and M3 (respectively).

Actually, models M2 and M3 have the same 5-level grid structure of model M1, except in the jet material ejected between times $t_1 = 100$ and $t_2 = 140$ yr. We label the material ejected at times $t_1 \le t \le t_2$ with a passive scalar, for which we integrate a passive advection equation. We then allow 3 (for model M2) or 6 (model M3) extra levels of grid refinement in the region of the flow with the appropriate value for the passive scalar.

This is illustrated in Fig. 2, where we show the stratifications of the density, the temperature and the passive scalar for a $t = 160$ yr time-integration. From this figure, it is clear that the second internal working surface (counting from the position of the source), located at a distance $x \approx 2.8 \times 10^{16}$ cm from the source, is composed of material in which the higher refinements are allowed (in models M2 and M3). In the following sections we focus on a description of the $t = 160$ yr flow structure of this particular internal working surface.

4. The flow structure of an internal working surface

In Fig. 3, we show the density stratifications obtained after a $t = 160$ yr time-integration for our "high spatial resolution" working surface (located at $x \approx 2.8 \times 10^{16}$ cm in Fig. 2, see the discussion at the end of Sect. 3). The corresponding grid structures (obtained in simulations M1-M3) are shown in Fig. 4. From Figs. 3 and 4, it is clear that while the general configuration of the flow is similar in the three simulations, smaller scale structures appear for increasing spatial resolutions (i.e., from model M1 to M2, and from model M2 to M3).

In order to illustrate in more detail the differences between the flow stratifications obtained with the three spatial resolutions, we show cuts along a line parallel to the symmetry axis, at a radius $r = 10^{15}$ cm (in other words, at a distance from the axis equal to 1/2 of the initial jet radius). Figures 5, 6 show the dependence (along these cuts) on distance x from the source (measured parallel to the jet axis) of the temperature, number density (of atoms and ions), electron density and ionization fraction.

In Fig. 5, we see that the temperature (along the $r = 10^{15}$ cm cuts described above) shows sharper features as one goes from model M1 to model M3. While model M1 shows a very diffuse structure, models M2 and M3 both show a two-peaked structure (with the peaks corresponding to the regions just behind the two shocks of the working surface), separated by a plateau

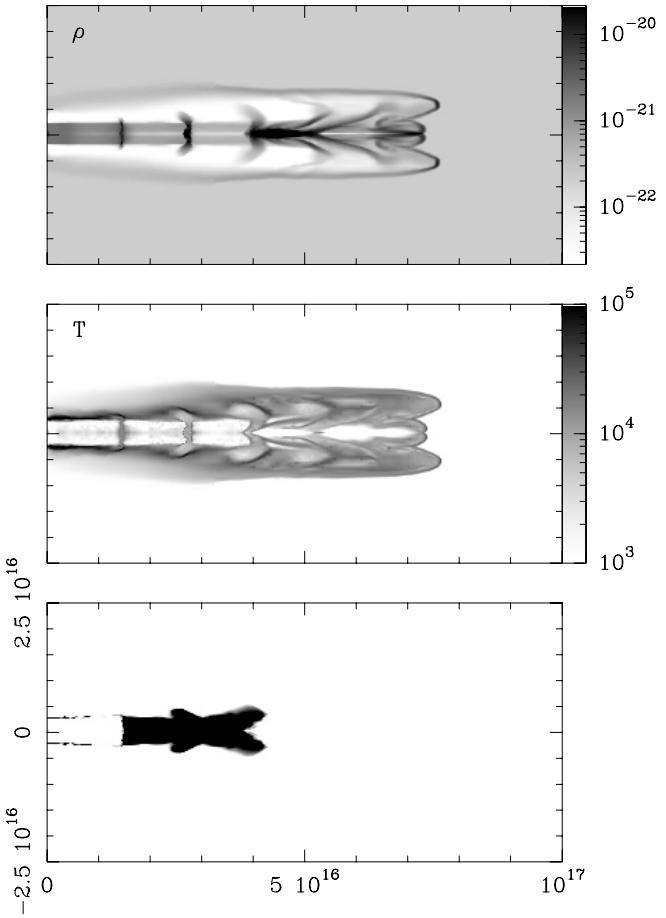

Fig. 2. Logarithmic density (*top*, with a bar giving the density in g cm^{-3}) and temperature (*centre*, with a bar giving the temperature in K) stratifications obtained from the M2 simulation (see the text) for a $t = 160$ yr time-integration. The *bottom plot* shows the stratification of the advected scalar (described in the text), with the dark regions corresponding to the spatial extent of the region in which the higher grid resolutions are allowed (in models M2 and M3, see the text). The abscissa corresponds to the outflow axis, and the ordinate corresponds to the cylindrical radius (which has been reflected in order to produce the displayed plots). Both axes are labeled in cm.

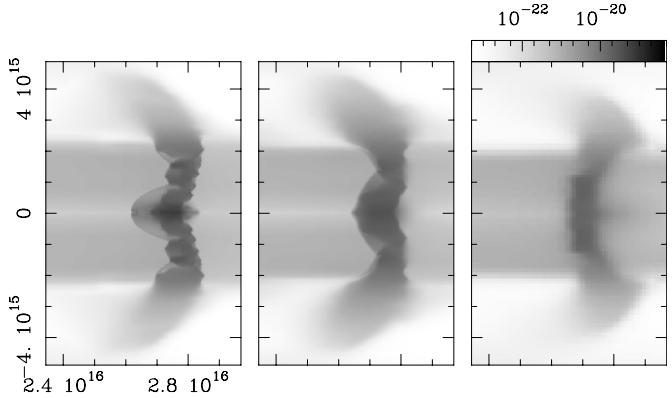

Fig. 3. Logarithmic density stratifications (with a bar giving the density in g cm^{-3}) for the region around the "high resolution" internal working surface (see the text and Fig. 2) obtained from models M1 (*right*), M2 (*centre*) and M3 (*left*) for a $t = 160$ yr time-integration.

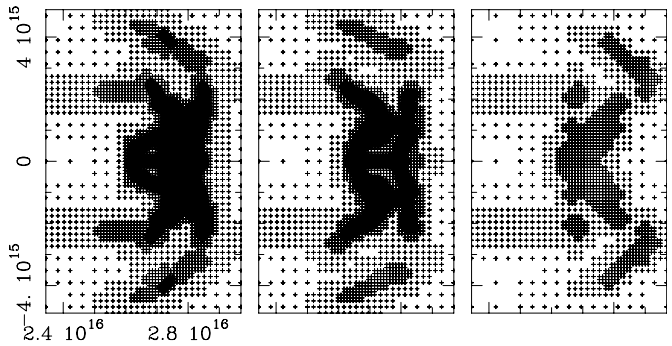

Fig. 4. Adaptive grid structures for the region around the "high resolution" internal working surface (see the text and Figs. 2 and 3) obtained from models M1 (*right*), M2 (*centre*) and M3 (*left*) for a $t = 160$ yr time-integration.

with a temperature of $\approx 10^4$ K. In these cuts, the width (along the axis) of the working surface is smaller in model M3 than in M2, though the reverse is true for cuts at other radii. As can be seen from the 2D density stratification of Fig. 3, the working surface is axially broader in model M3 (compared to M2) both on the symmetry axis and on the edge of the jet beam.

In Fig. 5, we also see that even though the stratifications differ in detail, the density n (of atoms+ions, along the $r = 10^{15}$ cm cuts) has similar values (to within ∼20%) in the three simulations. The electron density n_e, however, shows substantially higher values in model M3, as can be seen in Fig. 6. Finally, the ionization fraction $f = n_e/n$ and OII ionization fraction $f_{OII} = n_{OII}/n_O$ show a qualitatively similar structure in M2 and M3 (though higher values are obtained for model M3), as can be seen in Fig. 6.

The stratifications shown in Figs. 5, 6 correspond to axial cuts at an $r = 10^{15}$ cm cylindrical radius. In order to illustrate the results obtained along other axial cuts, in Fig. 7 we show density cuts at $r = 0$, 1.5×10^{15} cm and 3×10^{15} cm (corresponding to the symmetry axis, and to 3/4 and 3/2 of the initial jet radius, respectively) obtained from the three computed models. In this

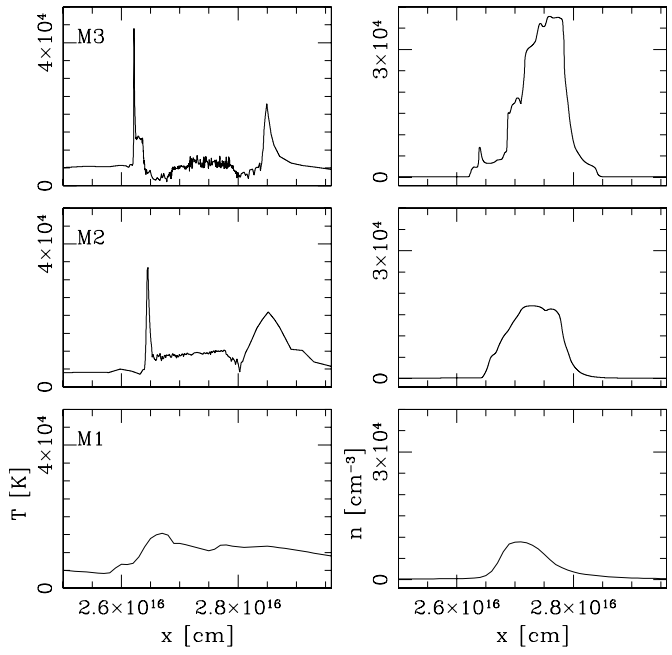

Fig. 5. Cuts along the outflow direction at a $r = 10^{15}$ cm cylindrical radius of the temperature (*left*) and ion+atom number density (*right*) stratifications of the internal working surface shown in Fig. 3. The results for the $t = 160$ yr time frames of simulations M1, M2 and M3 are shown.

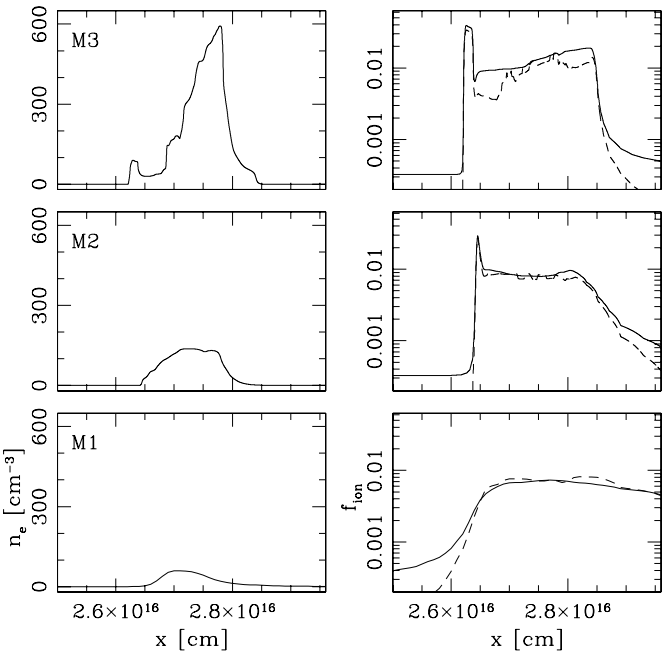

Fig. 6. *Left*: cuts along the outflow direction at a $r = 10^{15}$ cm cylindrical radius of the electron density stratification of the internal working surface shown in Fig. 3. *Right*: similar cuts, but of the ionization fraction n_e/n (solid lines) and oxygen ionization fraction n_{OII}/n_O (dashed lines) stratifications. The results for the $t = 160$ yr time frames of simulations M1, M2 and M3 are shown.

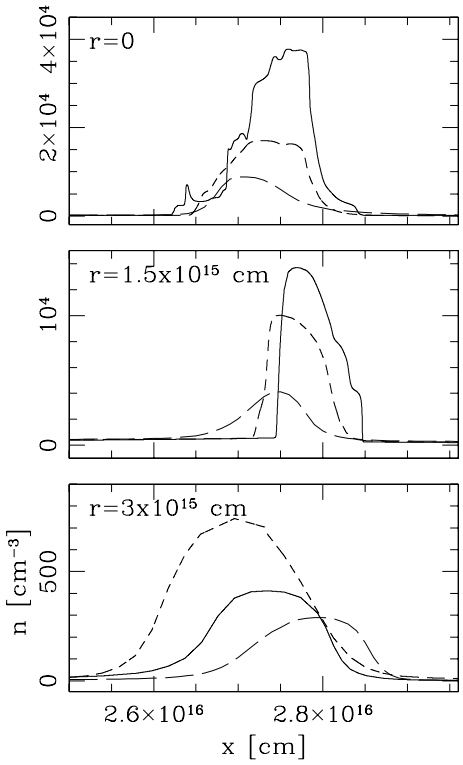

Fig. 7. Ion+atom density cuts along the outflow direction at $r = 0$ (i.e., along the symmetry axis, *top*), $r = 1.5 \times 10^{15}$ cm (*centre*) and $r = 3 \times 10^{15}$ cm (*bottom*). The results for the $t = 160$ yr time frames of simulations M1 (long dashes), M2 (short dashes) and M3 (solid lines) are shown.

figure, we see that both spatial offsets (along the symmetry axis) as well as substantial changes in the height of the density maxima are obtained as a function of resolution for the three chosen cuts.

It is clear that for all flow variables, the low resolution model M1 shows much smoother structures than in the other two models, and has values for the flow variables that differ more strongly (as compared to the differences between M2 and M3). This is not surprising given the fact that in model M1 the $\sim 10^{16}$ cm separation between the two working surface shocks is only resolved with ∼10 grid points (as compared to ∼80 points for model M2 and ∼640 points for M3).

5. The Hα and [O I] 6300 emission

Finally, we have used the temperature, electron density and number densities of HI, HII and OI (from the $t = 160$ yr flow stratification of the internal working surface) in order to compute the Hα and [O I] 6300 emission coefficients. The Hα emission was computed considering the recombination cascade and the $n = 1 \rightarrow 3$ electron collisional excitations. The [O I] 6300 emission coefficient was computed by solving the appropriate 5-level atom problem.

We have then integrated these emission coefficients along lines of sight in order to compute emission maps for the two emission lines. These maps were computed assuming that the outflow axis lies on the plane of the sky. The resulting emission maps are shown in Figs. 8 (Hα) and 9 ([O I] 6300).

Figures 8 and 9 show that while the Hα map has relatively strong emission from the bow shock wings, the [O I] 6300 emission is strongly dominated by the shocks within the beam of the jet. We again find that while the results are qualitatively similar for the three numerical resolutions, smaller scale structures appear as one goes from model M1 to model M3.

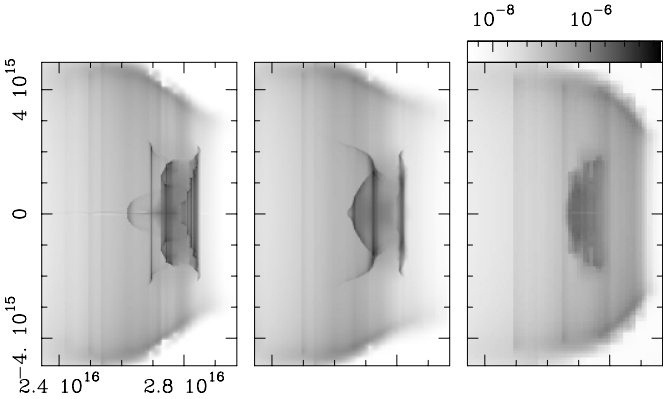

Fig. 8. Hα intensity maps for the "high resolution" internal working surface (see the text and Fig. 3), obtained assuming that the outflow axis lies on the plane of the sky. The results obtained from our three simulations (M1: *right*, M2: *centre* and M3: *left*) are shown. The bar gives the logarithmic greyscale in erg cm^{-2} s^{-1} sterad^{-1}.

It is interesting to note that the observed HH jets typically have a diameter of ∼0.″5. Therefore, even with the highest currently possible resolutions of optical observations (which have values of ∼0.″1) the radius of the jet beam is only marginally resolved. Because of this, differences such as the ones that we obtain between our three models might be irrelevant when one attempts a comparison with the observations.

In order to quantify the differences between the three models, we have carried out a volume integral of the emission coefficients (within a domain that includes all of the emission of the internal working surface) in order to calculate the Hα and [O I] 6300 luminosities ($L_{H\alpha}$ and $L_{[O\,I]\,6300}$, respectively) of the

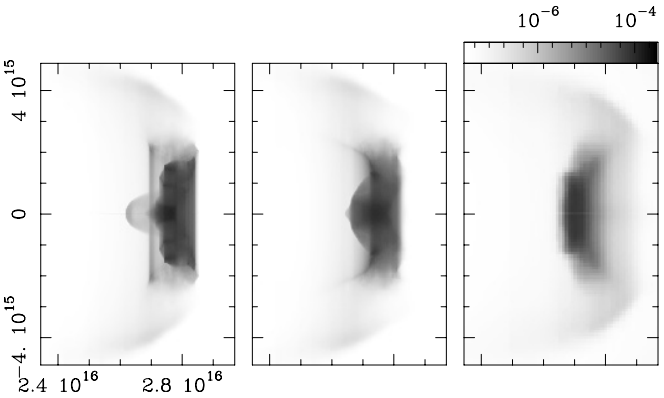

Fig. 9. [O I] 6300 intensity maps for the "high resolution" internal working surface (see the text and Fig. 3), obtained assuming that the outflow axis lies on the plane of the sky. The results obtained from our three simulations (M1: *right*, M2: *centre* and M3: *left*) are shown. The bar gives the logarithmic greyscale in erg cm^{-2} s^{-1} sterad^{-1}.

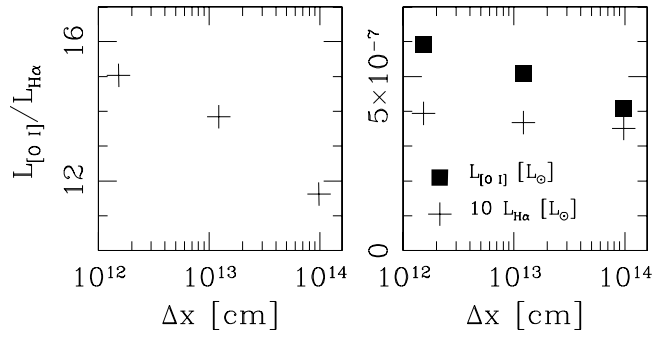

Fig. 10. [O I] 6300 and Hα (multiplied by a factor of 10) luminosities (given in solar luminosities, *right*) and the [O I] 6300/Hα line ratio (*left*) of the "high resolution" internal working surface (see the text and Fig. 3) as a function of the maximum resolution Δx of the adaptive grids of models M1 (points at $\Delta x = 9.766 \times 10^{13}$ cm), M2 (points at $\Delta x = 1.221 \times 10^{13}$ cm) and M3 (points at $\Delta x = 1.526 \times 10^{12}$ cm).

knot. The results are shown in Fig. 10, in which we plot the resulting luminosities as a function of the spatial resolution of the simulation.

Quite remarkably, we find that the emission line luminosities show a very shallow dependence on the resolution of the simulation. The Hα luminosity shows a change of only 12% over the ∼2 orders of magnitude in resolution covered by our simulations. The [O I] 6300 simulation shows a 25% change from model M1 to M2, and a 16% change from M2 to M3. The $L_{[\mathrm{O\,I}]\,6300}/L_{\mathrm{H}\alpha}$ line ratio appears to be stabilizing at a value of ≈15 for the higher resolution models.

We should note that this [O I] 6300/H$\alpha \approx 15$ line ratio is very high in comparison with values obtained, e.g., for the brighter knots along the HH 34 jet (as can be seen even from the original paper on this jet of Reipurth et al. 1986, who obtain a value of ∼2 for this line ratio). This difference is in principle not a fundamental problem, as no effort has been made in the the present work to choose a variability that in detail reproduces the properties of this particular jet (see Raga et al. 2002b, for a description of multi-sinusoidal mode models for this particular jet, and Massaglia et al. 2005, for a discussion of alternative functional forms of the ejection time-variability).

6. Conclusions

We have computed three simulations spanning a factor of 64 in spatial resolution of a single variable ejection velocity, radiative jet flow. The simulations are carried out with a binary adaptive grid, in which the higher resolutions are only allowed in one of the internal working surfaces of the jet flow. The subsequent study of the results is then limited to this particular working surface, and to a single time frame (the working surface being centered at $x \approx 2.8 \times 10^{16}$ cm at the chosen, $t = 160$ yr integration time).

As can be seen from Fig. 2, the "high resolution working surface" at $t = 160$ yr is relatively far away from the head of the jet. It has been previously shown that the successive internal working surfaces produced by a periodic ejection time-variability follow almost identical time evolutions (until they start catching up with the leading head of the jet, see, e.g., Masciadri et al. 2002). Therefore, all of the internal working surfaces along the jet should have a time-evolution similar to the one of the "high resolution working surface", so that the particular choice of which working surface to follow at high resolution is not important.

We have also limited the comparison between the solutions at different resolutions to a single time-frame. Clearly, different results would be obtained for other time-frames, and the comparisons between the $t = 160$ yr flow stratifications (shown in the present paper) should only be taken as an illustration of the magnitude of the differences obtained between simulations at different resolutions.

The three computed simulations correspond to resolutions of the jet radius by 20 (model M1), 163 (M2) and 1310 (M3) grid points (at the highest resolution of the adaptive grid). We find that while the lowest resolution simulation (M1) shows very smooth structures, the other two simulations (M2 and M3) show qualitatively similar flow variable stratifications (see, e.g., Figs. 3 and 4). However, we do not obtain a convergence to a given numerical solution of the gasdynamic equations, as smaller scale structure is obtained for each of the two factor 8 increases in resolution (from model M1 to M2, and from M2 to M3, respectively).

We have carried out predictions of intensity maps for the Hα and the [O I] 6300 emission lines. The maps again show a systematic increase in smaller scale structures as one goes to higher numerical resolutions. However, we find that the emission integrated over all of the emitting volume of the internal working surface is surprisingly stable as a function of resolution of the simulations.

In particular, we find that the integrated Hα luminosity changes only very slowly as a function of resolution. The [O I] 6300 luminosity changes by 25% from model M1 to M2, but only by 16% from model M2 to M3. Therefore, it appears that model M2 gives the correct [O I] 6300 luminosity to within an error of ∼20%, which appears to be an acceptable error from the point of view of predictions of emission line intensities meant for comparisons with observations of HH objects.

We would then conclude that numerical simulations in which the jet radius is resolved with ∼100 → 200 grid points are appropriate for carrying out acceptably reliable predictions of emission line intensities of the successive knots (i.e., internal working surfaces) along a variable ejection velocity outflow. However, this conclusion is based on an analysis of a single set of jet parameters. It will of course be necessary to carry out studies of a wider parameter range in order to validate an extended grid of variable, radiative jet models.

An important point of course is whether or not it is always worth to go for the highest possible resolution. The computations described in the present paper were carried out in a single, Intel(R) Xeon(TM) MP CPU 2.80 GHz processor. Models M1, M2 and M3 ran in CPU times of approximately 2 h, 2 days and 2 months, respectively. Therefore, with the present computational setup it might be realistic to run grids of models with the resolution of model M2, but not with the resolution of M3 (though one could of course carry out a reduced set of simulations at the resolution of this model). This situation will of course improve with simulations carried out with a parallel code running in multi-processor machines.

Acknowledgements. The work of A.R., P.K. and A.E. was supported by the CONACyT grants 43103-F and 46828-F, the DGAPA (UNAM) grant IN 113605 and the "Macroproyecto de Tecnologías para la Universidad de la Información y la Computación" (Secretaría de Desarrollo Institucional de la UNAM, Programa Transdisciplinario en Investigación y Desarrollo para Facultades y Escuelas, Unidad de Apoyo a la Investigación en Facultades y Escuelas). The present work was supported in part by the European Community's Marie Curie Actions – Human Resource and Mobility within the JETSET (Jet Simulations, Experiments and Theory) network under contract MRTN-CT-2004 005592. We thank Enrique Palacios and Martín Cruz for supporting the servers in which the calculations of this paper were carried out. Finally, we thank an anonymous referee for his/hers very relevant comments.

Appendix A: Ionization, recombination and charge exchange coefficients

This appendix describes the rate coefficients used for the atomic/ionic network used in the gasdynamic simulations. The ionization, recombination and charge exchange coefficients listed in Table 1 are either given with the Arrhenius interpolation formula:

$$r(T) = a_1\, T^{a_2}\, \mathrm{e}^{a_3/T}, \tag{A.1}$$

or with the interpolation formula of Aldrovandi & Péquignot (1973, 1976):

$$r(T) = a_1 \left(\frac{T}{10^4}\right)^{-a_2} + a_3 T^{-3/2} \times \exp\left(-a_4/T\right)\left[1 + a_5 \exp\left(-a_6/T\right)\right], \tag{A.2}$$

with the temperature T given in K.

In the case of rates given in terms of Eq. (A.1), the entry in the second column of Table 1 reads "1: a_1, a_2, a_3". For the rates given in terms of Eq. (A.2), the corrseponding entry in the second column of Table 1 reads "2: a_1, a_2, a_3, a_4, a_5, a_6".

References

Aldrovandi, S. M. V., & Péquignot, D. 1973, A&A, 25, 137
Aldrovandi, S. M. V., & Péquignot, D. 1976, A&A, 47, 321
Biro, S. 1996, MNRAS, 278, 990
Biro, S., & Raga, A. C. 1994, ApJ, 434, 221
Blondin, J. M., Konigl, A., & Fryxell, B. A. 1989, ApJ, 337, L37
Cox, D. P. 1970, Ph.D. Thesis, Univ. of California, San Diego, USA
Downes, T. P., & Ray, T. P. 1998, A&A, 331, 1130
Falle, S. A. E. G., & Raga, A. C. 1993, MNRAS, 261, 573
Falle, S. A. E. G., & Raga, A. C. 1995, MNRAS, 272, 785
Hartigan, P., & Raymond, J. C. 1993, ApJ, 409, 705
Hartigan, P., Raymond, J. C., & Hartmann, L. 1987, ApJ, 316, 723
Innes, D. E., Giddings, J. R., & Falle, S. A. E. G. 1987a, MNRAS, 226, 67
Innes, D. E., Giddings, J. R., & Falle, S. A. E. G. 1987b, MNRAS, 226, 1021
Kajdič, P., Velázquez, P. F., & Raga, A. C. 2006, RMxAA, 42, 217
Kössl, D., & Müller, E. 1988, A&A, 206, 204
Lim, A. J., Rawlings, J. M. C., & Williams, D. A. 1999, MNRAS, 308, 1126
Lim, A. J., Rawlings, J. M. C., & Williams, D. A. 2001, MNRAS, 376, 336
Masciadri, E., Velázquez, P. F., Raga, A. C., Cantó, J., & Noriega-Crespo, A. 2002, ApJ, 573, 260
Massaglia, S., Mignone, A., & Bodo, G. 2005, A&A, 442, 549
Osterbrock, D. E. 1989, Astrophysics of gaseous nebulae and active galactic nuclei (Univ. Science Books)
Raga, A. C. 1988, ApJ, 335, 820
Raga, A. C., Cantó, J., Binette, L., & Calvet, N. 1990, ApJ, 364, 601
Raga, A. C., Navarro-González, R., & Villagrán-Muniz, M. 2000, RMxAA, 36, 67
Raga, A. C., Sobral, H., Villagrán-Muniz, M., Navarro-González, R., & Masciadri, E. 2001, MNRAS, 324, 206
Raga, A. C., de Gouveia dal Pino, E. M., Noriega-Crespo, A., Mininni, P., & Velázquez, P. F. 2002a, A&A, 392, 267
Raga, A. C., Velázquez, P. F., Cantó, J., & Masciadri, E. 2002b, A&A, 395, 647
Raga, A. C., Riera, A., Masciadri, E., et al. 2004, AJ, 127, 1081
Raga, A. C., Williams, D. A., & Lim, A. J. 2005, RMxAA, 41, 137
Reipurth, B., Bally, J., Graham, J. A., Lane, A. P., & Zealy, W. J. 1986, A&A, 164, 51
Seaton, M. J. 1959, MNRAS, 119, 81
Shapiro, P. R., & Moore, R. T. 1976, ApJ, 207, 460
Smith, M. D., & Rosner, A. 2005, MNRAS, 357, 1370
Smith, M. D., Suttner, G., & Yorke, H. W. 1997, A&A, 323, 223
Sobral, H., Villagrán-Muniz, M., Navarro-González, R., & Raga, A. C. 2000, App. Phys. Lett., 77, 3158
Velázquez, P. F., Sobral, H., Raga, A. C., Villagrán-Muniz, M., & Navarro-González, R. 2001, RMxAA, 37, 87